

The impact of sloshing on the intra-group medium and old radio lobe of NGC 5044

Ewan O’Sullivan^{*1}, Laurence P. David¹, Jan M. Vrtilik¹

¹ *Harvard-Smithsonian Center for Astrophysics, 60 Garden Street, Cambridge, MA 02138*

Accepted 2013 October 7; Received 2013 October 2; in original form 2013 September 22

ABSTRACT

We present temperature and abundance maps of the central 125 kpc of the NGC 5044 galaxy group, based on a deep *XMM-Newton* observation. The abundance map reveals an asymmetrical abundance structure, with the centroid of the highest abundance gas offset ~ 22 kpc northwest of the galaxy centre, and moderate abundances extending almost twice as far to the southeast than in any other direction. The abundance distribution is closely correlated with two previously-identified cold fronts and an arc-shaped region of surface brightness excess, and it appears that sloshing, induced by a previous tidal encounter, has produced both the abundance and surface brightness features. Sloshing dominates the uplift of heavy elements from the group core on large scales, and we estimate that the southeast extension (the tail of the sloshing spiral) contains at least $1.2 \times 10^5 M_{\odot}$ more iron than would be expected of gas at its radius. Placing limits on the age of the encounter we find that if, as previously suggested, the disturbed spiral galaxy NGC 5054 was the perturber, it must have been moving supersonically when it transited the group core. We also examine the spectral properties of emission from the old, detached radio lobe southeast of NGC 5044, and find that they are consistent with a purely thermal origin, ruling out this structure as a significant source of spectrally hard inverse-Compton emission.

Key words: galaxies: abundances — galaxies: active — galaxies: clusters: intracluster medium — galaxies: elliptical and lenticular, cD — galaxies: groups: individual (NGC 5044) — X-rays: galaxies

1 INTRODUCTION

The high throughput and angular resolution of the current generation of X-ray telescopes (*XMM-Newton* and *Chandra*) has revealed a wealth of structure in the hot intergalactic medium of galaxy groups and clusters. This has facilitated the study of a number of astrophysical processes, most notably AGN feedback and mergers. One of the first classes of structures recognised in early *Chandra* observations were cold fronts, well-defined discontinuities in X-ray surface brightness in which the inner, brighter side of the front is cooler and denser (e.g., Markevitch et al. 2000; Vikhlinin et al. 2001). Although cold fronts are often found in ongoing mergers, in many cases such fronts are observed in apparently relaxed groups and clusters, taking the form of arcs or spirals around the cool core (e.g., Markevitch & Vikhlinin 2007). These are thought to be formed by the process of sloshing, in which the passage of a lower-mass subcluster or subgroup falling through the main cluster transfers angular momentum to the intra-cluster medium (ICM), setting it oscillating within the cluster potential (Markevitch et al. 2001). This oscillation produces an expanding spiral pattern of discontinuities, as lower entropy gas from the cluster core is lifted outward,

cooling adiabatically to maintain pressure equilibrium with its new surroundings. This process has been extensively modelled via numerical simulations (e.g., Ascasibar & Markevitch 2006; ZuHone et al. 2011; Roediger et al. 2011) and studied in detail in a number of groups and clusters (see, e.g., references in Roediger et al. 2011).

The cool gas transported out of the group or cluster core by the sloshing motions has typically been enriched by supernovae in the central dominant elliptical or cD galaxy, and these metals are also transported out to larger radii (e.g., Simionescu et al. 2010; de Plaa et al. 2010; Roediger et al. 2011; Gastaldello et al. 2013; Ghizzardi et al. 2013; Canning et al. 2013). Merger-induced sloshing is therefore an important process for the redistribution of metals from galaxies out into the ICM, alongside uplift by the jets of group and cluster-central active galaxies (e.g., Sanders et al. 2004; Kirkpatrick et al. 2009; O’Sullivan et al. 2011).

NGC 5044 is the X-ray brightest group in the sky, and at a redshift of $z=0.00928$, has an angular scale ($1''=185$ pc) well-suited for the study of structures in its intra-group medium (IGM). The position of peak X-ray surface brightness agrees well with the optical centroid of the galaxy, but *ROSAT* observations showed that despite the generally relaxed and regular appearance of the extended IGM, the galaxy is offset from the centroid of the large-scale X-ray emission, suggesting some degree of disturbance (David et al.

* E-mail: ejos@head.cfa.harvard.edu

1994). The *ROSAT* data also showed that the cool core is asymmetrical, with a tail or plume of cool gas extending southeast. A joint *Chandra* and *XMM* analysis found evidence of multiphase gas within the central 30 kpc, and identified a cold front northwest of the core (Buote et al. 2003a), and Gastaldello et al. (2009) later identified an inner cold front to the southeast. The presence of these two fronts, their relative distances from the galaxy centroid ($\sim 150''$ and $350''$ for the SE and NW fronts respectively) and the $\sim 150 \text{ km s}^{-1}$ offset between NGC 5044 and the group mean velocity (Cellone & Buzzoni 2005; Mendel et al. 2008) lead to the suggestion that the group is sloshing (Gastaldello et al. 2009; David et al. 2009).

Deeper *Chandra* observations revealed numerous small cavities in the IGM core, indicating that NGC 5044 has undergone several recent AGN outbursts (David et al. 2009, 2011). The isotropic distribution of the cavities suggests that gas motions within the core have produced a highly structured IGM with a wide range of abundances, mixed with bubbles of relativistic plasma inflated by the AGN jets. While gas motion in the core may be driven by the heating effects of the AGN, Giant Metrewave Radio Telescope (GMRT) observations at 235 MHz show the impact of the sloshing motions on larger scales; a one-sided jet undergoes two $\sim 90^\circ$ bends around the inner SE cold front, which also abuts a detached radio lobe. Neither lobe or jet are detected at higher frequencies, indicating an ultra-steep spectral index ($\gtrsim 1.6$) and probable great age.

David et al. (2011) consider the sloshing and suggest NGC 5054, a disturbed spiral galaxy $\sim 27'$ SE of NGC 5044, as the likely perturber. A deep *XMM-Newton* observation was analysed by Gastaldello et al. (2013) who identified a surface brightness excess east of the core, at larger radii than the cold fronts, and noted that this feature was predicted by sloshing simulations. They argue that the alignment of the fronts and excess suggests that our line of sight is almost parallel to the orbital plane of the perturber, and consistent with the perturber’s current location being east of the group core.

In this paper we use a deep, ~ 100 ks *XMM* observation to investigate the temperature and abundance distributions of the IGM on large scales, and the impact of sloshing on the metal distribution of the group. The paper is organised as follows: In § 2 we describe the *XMM* observation, the data reduction and spectral extraction methods used in our analysis; in § 3 we present the temperature and abundance maps of the group, examine the change in IGM properties across the cold fronts, and examine the consistency of our results with *Chandra* observations; in § 4 we examine the X-ray emission from the region of the detached radio lobe, and search for evidence of non-thermal emission; finally, in § 5 we discuss our results in the context of the enrichment of the IGM and the impact of sloshing on the radio structures.

Throughout the paper we report uncertainties at the 68% confidence limit. We adopt a cosmology with $H_0=70 \text{ km s}^{-1} \text{ Mpc}^{-1}$, $\Omega_m=0.3$ and $\Omega_\Lambda=0.7$. Abundances were measured relative to the abundance table of Grevesse & Sauval (1998).

2 OBSERVATIONS AND DATA REDUCTION

NGC 5044 was observed by *XMM-Newton* on 2008 December 27 (ObsID 0554680101) for a total of 128,819s. The EPIC instruments operated in full frame mode with the thin optical blocking filter. The data were reduced and analysed using the *XMM* Science Analysis System (SAS v12.0.1). Times when the total count rate deviated from the mean by more than 3σ were excluded, leaving effec-

tive exposure times of 71 ks (EPIC-pn) and 98 ks (MOS). Diffuse X-ray emission from the intra-group medium (IGM) of NGC 5044 fills the field of view of the EPIC instruments. This makes accurate scaling and correction of blank-sky background data to match the observation dataset difficult, and we therefore chose to model the background, except when examining a region of limited size, where a local background region could be used.

When modelling the background, we took two approaches. Where a limited number of spectra were to be fitted (for example in radial profiles) we used the *XMM*-Extended Source Analysis Software (ESAS) and the general model suggested by Snowden et al. (2004). Point sources identified using the CHEESE-BANDS task are excluded, and spectra and responses for each region were extracted. Chip 5 of MOS 2 was found to be in an anomalous state with mildly enhanced background, and was excluded from the ESAS analysis. An additional *ROSAT* All-Sky Survey (RASS) spectrum, extracted from an annulus $1.75\text{--}2.25^\circ$ ($\sim 1.16\text{--}1.5$ Mpc) from the group centre using the HEASARC X-ray Background Tool¹ was also included to help constrain the soft X-ray background. All spectra were fitted simultaneously in XSPEC 12.8.0 (Arnaud 1996). Energies outside the range 0.3–10.0 keV (MOS) and 0.4–7.2 keV (pn) were ignored.

The particle component of the background was partially subtracted using particle-only datasets scaled to match the event rates in regions of the detectors which fall outside the field of view. Out-of-time (OOT) events in the EPIC-pn data were statistically subtracted using scaled OOT spectra. The remainder of the particle background was modelled with a powerlaw whose index was linked across all annuli. As this element of the background is not focused by the telescope mirrors, diagonal Ancillary Response Files (ARFs) were used. The instrumental Al $K\alpha$ and Si $K\alpha$ fluorescence lines were modelled using Gaussians whose widths and energies were linked across all annuli, but with independent normalisations. The X-ray background was modelled with four components whose normalisations were tied between annuli, scaling to a normalisation per square arcminute as determined by the PROTON-SCALE task. The cosmic hard X-ray background was represented by an absorbed powerlaw with index fixed at $\Gamma=1.46$. Thermal emission from the Galaxy, local hot bubble and/or heliosphere was represented by one unabsorbed and two absorbed APEC thermal plasma models with temperatures of 0.1, 0.1 and 0.25 keV respectively. The normalisations of the APEC models were free to vary relative to one another. Absorption was represented by the WABS model, fixed at the Galactic column density ($n_H=4.87 \times 10^{20} \text{ cm}^{-2}$, taken from the Leiden/Argentine/Bonn survey, Kalberla et al. 2005). The RASS spectrum was fitted using only the X-ray background components.

Since spectral extraction in ESAS is slow, and fitting is performed simultaneously across multiple regions, this approach is unsuitable for spectral mapping, where large numbers of spectra must be extracted and fitted. We therefore adopted an alternative method when creating spectral maps. We extracted spectra using standard SAS tools, removing bad pixels and columns, and filtering the events lists to include only those events with FLAG = 0 and patterns 0–12 (for the MOS cameras) or 0–4 (for the PN). An out-of-time (OOT) events list was created and scaled OOT spectra were used to statistically subtract the OOT contribution during analysis.

To reduce the computational time required to create spectra and responses, we used a 8×8 grid of Redistribution Matrix Files

¹ <http://heasarc.gsfc.nasa.gov/cgi-bin/Tools/xraybg/xraybg.pl>

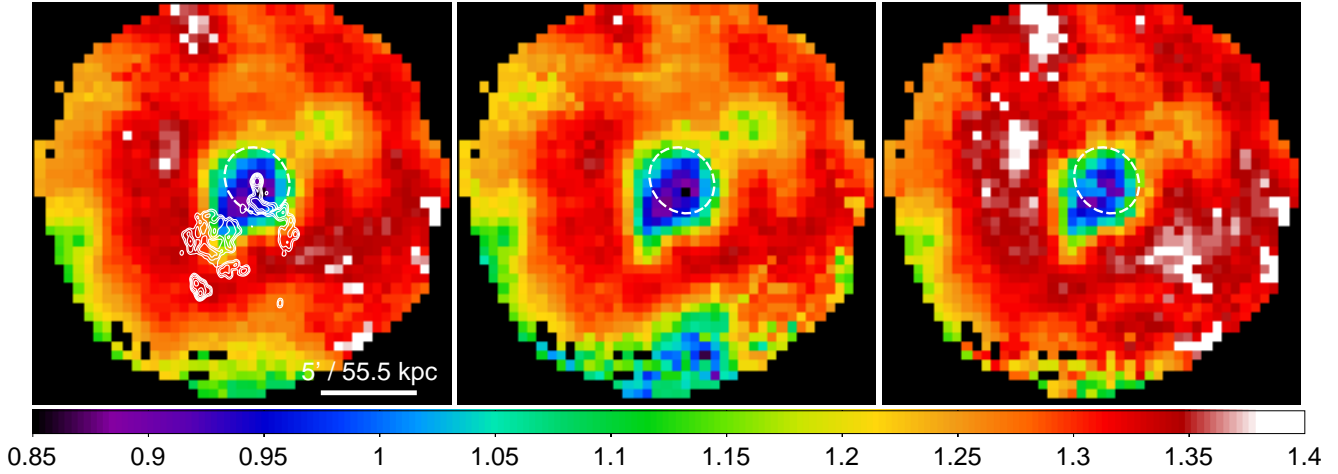


Figure 1. *XMM-Newton* projected temperature maps of NGC 5044, aligned with north up the page and west to the right. The left panel shows the best-fitting value, the centre and right panels the 1σ lower and upper bounds respectively. The dashed ellipse shows the D_{25} contour of NGC 5044. GMRT 235 MHz contours are overlaid in the left panel, with half-power beam width (HPBW) $\approx 22'' \times 16''$, the contour levels starting 3σ above the r.m.s. noise ($3\sigma = 0.75$ mJy beam $^{-1}$) and increasing in steps of factor two.

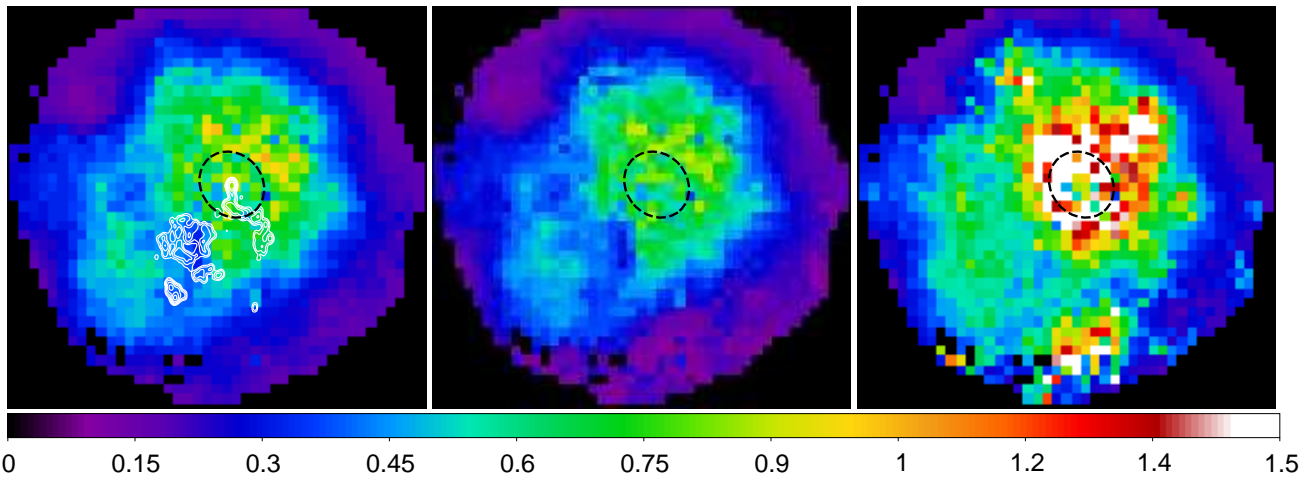


Figure 2. *XMM-Newton* projected abundance maps of NGC 5044, aligned with north up the page and west to the right. The left panel shows the best-fitting value, the centre and right panels the 1σ lower and upper bounds respectively. The D_{25} ellipse and GMRT 235 MHz contours are overlaid, as described in figure 1.

(RMFs) for each camera, assigning each spectrum an RMF based on its central position. We also used the EVIGWEIGHT task to weight each event based on its position in the detector, correcting for variations of effective area across the field of view. This allows a single on-axis ARF to be used for each instrument. As a result, the accuracy of the responses for each spectrum is slightly reduced, but we consider this an acceptable trade-off given the decrease in spectral extraction time and since features identified from the maps can later be confirmed using standard responses. The spectra for each region were then fitted using the same energy bands and essentially the same model as used in the ESAS fitting described above. No background subtraction was performed, so the powerlaw representing the particle background modelled the entirety of this component. Fitting was carried out in CIAO *Sherpa* v4.5 (Freeman et al. 2001).

3 SPECTRAL MAPS

In order to determine the large-scale two-dimensional projected distribution of abundance and temperature in NGC 5044, we created spectral maps of the system. We followed a process similar to that used for the *Chandra* observation (David et al. 2011) and in our previous *XMM* studies of groups (e.g., O’Sullivan et al. 2011). The field of view was divided into a grid of $30''$ -square pixels, whose centres correspond to the centres of circular spectral extraction regions. The radius of these circular regions was allowed to vary in steps of factor 1.4 between $15.9''$ and $2''$, with the aim of including at least 6000 net counts, summed over the three cameras. Since the background had not been modelled at this stage, it was approximated using blank-sky data, normalised to the observation data sets using the out of field of view events in the 2-7 keV band. Regions whose surface brightness was too low to provide 6000 net counts in the maximum extraction region were excluded from further analy-

sis. The spectral extraction regions can be larger than the pixel size, in which case neighbouring pixels will not be independent; in our *XMM* maps pixels less than $\sim 5'$ from the galaxy centroid are independent, but at larger radii the spectral extraction regions overlap. For this reason, and because of the nature of the background modelling approach used, the maps should be considered as tools for identifying regions of interest which can then be investigated and confirmed using standard spectral analysis techniques. Previous experience has shown that such maps are generally useful and reliable in this role (e.g., O’Sullivan et al. 2012; David et al. 2011; O’Sullivan et al. 2011, 2007)

Each spectrum was fitted using the background model described above, plus an absorbed APEC thermal plasma component representing the IGM. The resulting maps are shown in figures 1 and 2. Fits typically have reduced χ^2 values of 0.75-1.15. Uncertainties in the map temperatures are generally small, ~ 0.02 keV, equivalent to $\sim 1\%$ of the measured value. The exception is a patch on the southern edge of the map (most visible as a blue/green region in the centre panel of Figure 1) where uncertainties rise to $\sim 10\%$. This corresponds to the location of MOS2 chip 5, suggesting that the larger errors are caused by the enhanced background and altered background spectrum in this chip. Abundance uncertainties are higher, typically 0.05-0.1 Z_{\odot} , with larger uncertainties in the core and southern patch. In these regions, the 1σ upper uncertainties can be $>0.5Z_{\odot}$. However, the structures seen in both maps are clearly visible in the uncertainty maps.

The temperature map shows the extended, comma-shaped cool core (0.85-1 keV) surrounded by higher temperature regions particularly to the south and west. A trail of mid-temperature (~ 1.2 keV) material extends to the northwest. The inner edge of this region was detected by *Chandra* (David et al. 2009, 2011). On larger scales the highest temperatures (~ 1.35 keV) persist to radii of $\sim 10'$ (110 kpc) to the north and west, but are less extended to the south and east, declining outside $\sim 8'$ (90 kpc).

The abundance map confirms the presence of a low abundance region southeast of the core, coincident with the detached radio lobe seen at 235 MHz. This region is part of a band of mixed-abundance (0.3-0.45 Z_{\odot}) emission extending around the southeast quadrant of the galaxy between 3 and 5' (33-55 kpc) from the galaxy core, with a clump of somewhat higher abundance material ($\sim 0.65Z_{\odot}$) beyond it. The main high abundance region associated with the group core is offset to the northwest of the galaxy, with the abundance centroid $\sim 2'$ (22 kpc) from the optical centroid. However, the upper abundance uncertainties in and around the galaxy are large, probably owing to a combination of multi-temperature gas along the line of sight, multi-phase gas within spectral extraction regions, and uncertainties on the particle component of the background. Fitting multi-temperature (and probably multi-abundance) emission with single-temperature models will tend to bias the best-fit abundance low (Buote & Fabian 1998). However, it is clear that the abundance distribution is not centred on the galaxy, with the highest abundances offset to the northwest, but moderate abundances most extended to the southeast. Abundances decline to 0.1-0.2 Z_{\odot} outside 6-7' on the northeast, northwest and southwest sides, but remain enhanced out to $>9.5'$ in the southeast.

Figure 3 shows a comparison between X-ray surface brightness and the abundance map. The two cold fronts are marked; one $\sim 150''$ (28 kpc) southeast of the galaxy centre, the other $350''$ (65 kpc) northwest. There is also the arc of excess emission discovered by Gastaldello et al. (2013) which extends from due west, inside the northwest front, through north and around the east side of the galaxy. In the southeast quadrant it lies between

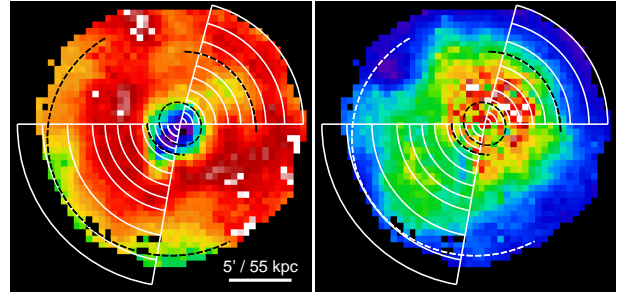


Figure 4. Regions used for extraction of the profiles shown in Figure 5, overlaid on the projected temperature (left) and abundance (right) maps. Dashed arcs indicate the cold fronts and outer limit of the southeast surface brightness excess, and the dashed ellipse marks the D_{25} optical contour of NGC 5044.

6-11' (66-122 kpc) from the galaxy centre. The arc is a highly significant surface brightness feature. Comparing the surface brightness in 80° regions to northwest and southeast, we find that the surface brightness to the southeast exceeds that to the northwest by $\sim 45\sigma$ between 400 and 600'' (see also Fig. 16 of Gastaldello et al. 2013). We find a strong correlation between these features and the abundance distribution. The highest abundances are found between the two cold fronts. The extended moderate-metallicity gas to the southeast of the galaxy reaches a radius very similar to the outer radius of the excess surface brightness arc, though the morphology of the two features does not correspond exactly. The moderate abundance material is more narrowly directed to the southeast than the surface brightness excess, which extends to the northeast and south into regions of low abundance. However, in general the abundance distribution compares reasonably closely with surface brightness, at least on arcminute scales, except in the core, where the lower temperatures and high densities produce a brightness peak at the centre of the cool core.

Correlation between surface brightness and the temperature distribution is less clear. Our map shows the moderate temperatures northwest of the galaxy which form the outer cold front, but as noted by David et al. (2011) the tail of the cool core extends across the southeast cold front. As noted previously, the southeast front lies just inside the detached radio lobe seen at 235 MHz.

3.1 Profiles across the cold fronts

To further examine the changes in IGM properties at the cold fronts and in the southeast surface brightness excess, we fitted spectral profiles extending from the galaxy optical centroid to the northwest and southeast. Spectra for the northwest profile were extracted between $270\text{--}345^\circ$ (where 0° is due north) and for the southeast profile between $90\text{--}170^\circ$, with radii chosen to match those of the surface brightness features. Since these profiles have a limited number of spectra (11 and 13 per camera for the NW and SE profiles), we use the ESAS background subtraction and modelling formalism, including standard *XMM* responses. The location of the profiles on the spectral maps is shown in Figure 4, and the resulting profiles of temperature and abundance are shown in Figure 5. Each partial annulus in the profiles contains $\gtrsim 20000$ net counts.

The profiles agree well with the maps, showing the greater extension of the cool core and abundance profile to the southeast, and the more compact abundance profile to the northwest, with a sharp decline at the cold front. Despite the underlying declining trend in

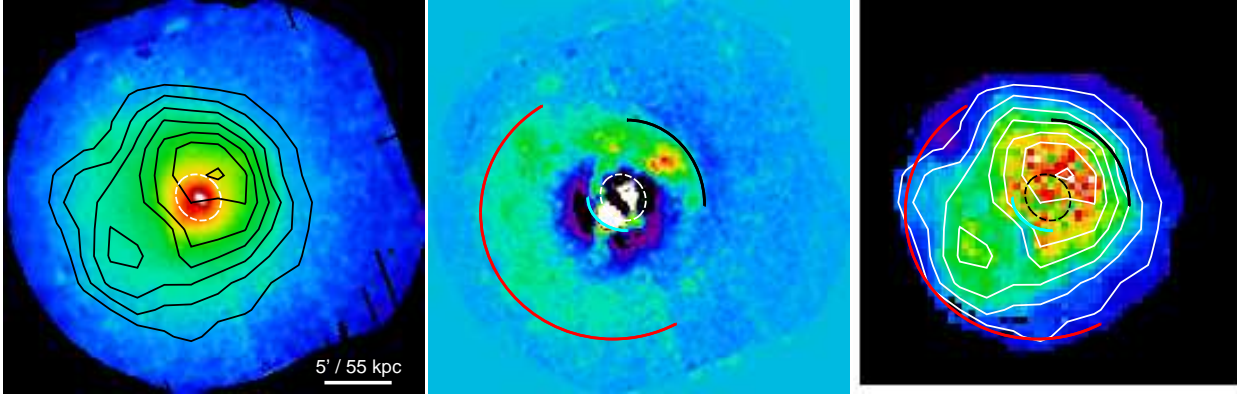


Figure 3. Comparison of X-ray surface brightness and abundance. The left panel shows a 0.3-2 keV MOS+pn image of NGC 5044, corrected for OOT events, with point sources removed and filled using the CIAO tool DMFILTH, and adaptively smoothed with a target signal-to-noise ratio of 20. The central panel shows the residuals after subtraction of a circular β -model, Gaussian smoothed with a $20''$ kernel. The right hand panel shows the projected abundance map. The three panels have the same scale and orientation, with north toward the top of the page and west to the right. The approximate D_{25} contour of NGC 5044 is marked by a dashed ellipse, and solid arcs indicate the locations of the cold fronts (SE in cyan, NW in black) and surface brightness excess feature (in red) identified in previous studies (David et al. 2009; Gastaldello et al. 2009, 2013). Smoothed abundance contours starting at $0.2Z_{\odot}$ and increasing in steps of $0.1Z_{\odot}$ are overlaid on the left and right panels.

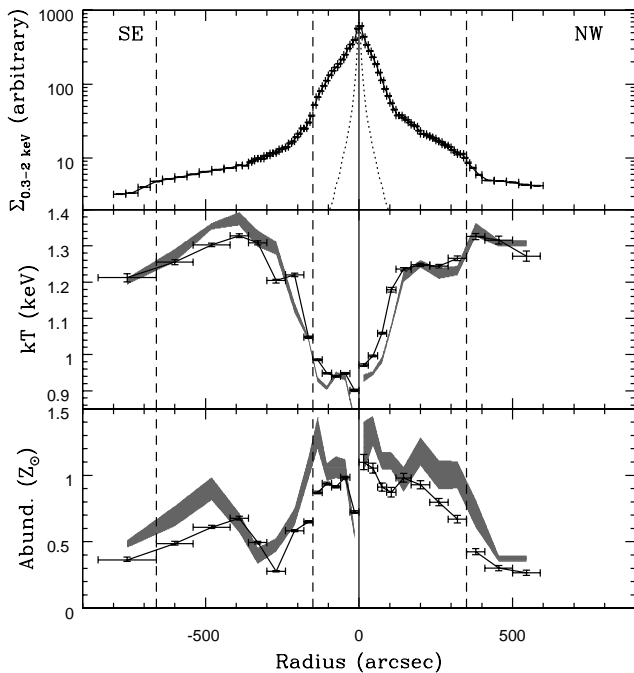


Figure 5. Profiles of projected 0.3-2 keV surface brightness, temperature and abundance extending northwest and southeast from the galaxy optical centroid, marked by the solid line at radius=0. Grey filled profiles mark the 1σ error region for the deprojected temperature and abundance profiles. Dashed lines mark the positions of cold fronts and the outer edge of the SE surface brightness excess. The X-ray surface brightness profiles have been corrected for exposure but no background has been subtracted. The dotted lines indicate the scaled K-band optical surface brightness profile of NGC 5044.

abundance with radius, it is clear that the jump in abundance across both cold fronts is significant, $0.24 \pm 0.04 Z_{\odot}$ at the northwest front and $0.22 \pm 0.03 Z_{\odot}$ at the southeast front. A temperature discontinuity is also visible across the northwest front, with an increase of 0.06 ± 0.01 keV outside a plateau of constant temperatures between

150-350''. Both fronts are visible as steepenings of the surface brightness profile, despite blurring by the *XMM* point spread function. Low abundances are found in the innermost bin of the southeast profile, and at 250-300'', the radius at which the detached radio lobe is observed and the abundance map shows a band of mixed-abundance gas. In both cases fitting a single-temperature model to complex multi-phase gas is probably biasing the abundance somewhat lower than the true value. The southeast abundance clump is visible as a subsidiary peak in abundance values at $\sim 400''$, associated with a flattening of the surface brightness profile. We note that enhanced abundances extend southeast to the edge of the *XMM* field of view, $\sim 800''$ (~ 150 kpc) from the galaxy centre, whereas $550''$ (100 kpc) northwest of the galaxy abundance has declined to a background level ($0.27 \pm 0.02 Z_{\odot}$ compared to $0.38 \pm 0.01 Z_{\odot}$).

Deprojected temperature and abundance profiles of the northwest and southeast profiles, fitted using the XSPEC PROJCT model, are also shown in Figure 5. The deprojected profiles are similar to their projected counterparts, with somewhat higher abundances throughout, and a slightly larger cool core. It is notable that in the southeast profile the temperature in the core is lowest at the galaxy centroid (radius 0), then rises to ~ 0.94 keV, then dips to 0.91 keV at $\sim 100''$. This behaviour is not visible in the projected profile, but is seen in the *XMM* temperature map and the *Chandra* temperature map of David et al. (2011).

Figure 6 shows the projected abundance profiles in the northwest and southeast quadrants, compared with equivalent profiles from 80° sectors to the northeast and southwest. Outside the core, the profiles from the (relatively undisturbed) NE and SW sectors agree reasonably well with one another in their general trend, though at radii beyond $300''$ there is some divergence and increasing scatter between radial bins. Taking the mean of these two profiles as an approximation of the ‘‘undisturbed’’ pre-sloshing abundance profile, we see that the NW profile has enhanced abundances between 200-350'', the region corresponding to the temperature plateau inside the NW surface brightness front. The SE abundance profile falls below the ‘‘undisturbed’’ mean profile out to $\sim 300''$, and is enhanced significantly above it at larger radii.

To test the impact of the adopted Galactic hydrogen col-

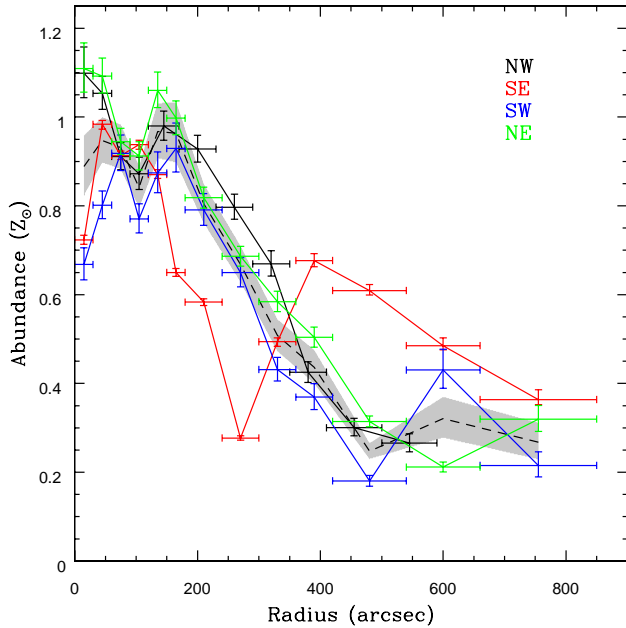


Figure 6. Projected metallicity profiles in 80° sectors extending northwest (black), southeast (red), southwest (blue) and northeast (red). The NW and SE profiles are the same as those shown in Figure 5. The grey hatched region and dashed line indicates the average abundance in the relatively undisturbed northeast and southwest sectors.

umn density on the profile fits, we refitted the southeast profile with the hydrogen column free to vary. The best fitting value, $(5.70 \pm 0.12) \times 10^{20} \text{ cm}^{-2}$, is $\sim 17\%$ greater than the weighted mean column along the line of sight to NGC 5044 (as derived using the HEASOFT task NH) but is within the scatter of values found in the $1^\circ \times 1^\circ$ region used to calculate the mean, and more similar to values found southeast of the group than to the northwest. The change in column has no impact on the shapes of the temperature or abundance profiles, and individual best-fit values generally change by less than their 1σ uncertainty. We therefore conclude that the choice of hydrogen column is acceptable and is not affecting our results.

We also attempted to test the impact of multi-temperature gas on our fits, since several studies have shown a requirement for multi-temperature models when fitting spectra from the core of NGC 5044 (e.g., Tamura et al. 2003; Buote et al. 2003a,b; David et al. 2009). Using the previous, shorter (~ 19 ks) *XMM* observation, Buote et al. (2003a) showed that even when deprojected, the emission within 30 kpc of the galaxy centroid was best fitted with a two-temperature model. David et al. (2009) found a similar result using a deep *Chandra* observation, showing that fitting in different energy bands produces different temperatures within 30 kpc but consistent temperatures at larger radii. It seems likely that the need for multi-temperature models arises in part from the temperature, abundance and density asymmetries of the IGM; previous studies have generally used radial profiles azimuthally averaged over the full 360° . Our deprojected northwest abundance profile is similar to the azimuthally averaged two-temperature Fe abundances profiles measured by Buote et al. (2003b) and falls significantly above their single-temperature profile. This suggests our choice of limiting angles for the profile reduces the degree of temperature variation in each annulus, accounting for much of the effect which Buote et al. required a two-temperature model to correct. However, David et al. (2011) find multi-temperature fits necessary even for small, homo-

geneous regions (as do we, see § 4) and it therefore seems likely that genuinely multi-phase gas may be present.

Unfortunately, our radial profile spectra are unable to constrain a second source component in addition to the one-temperature deprojected source and background components. When a second thermal model is included in the fit, its temperature and/or normalisation either become unphysical or are so poorly constrained as to be meaningless. Even with parameters linked between groups of bins we are unable to find a meaningful fit. We do not see the strong residuals around the Fe-L complex which are characteristic of single-temperature fits to multi-temperature emission (see e.g., Buote et al. 2003a, Fig. 9), supporting our view that our choice of regions has reduced the need for a more complex model. A thorough investigation of the impact of multi-phase gas which takes into account the asymmetries and discontinuities in the IGM probably requires a deeper observation. However, the fact that our fits do not require a second temperature component and agree reasonably well with the best previous abundance profiles leads us to conclude that they are reliable, at least outside the central 30 kpc.

3.2 Comparison with *Chandra*

Comparing our maps with those of David et al. (2011), we find that while the field of view and resolution of the *XMM* and *Chandra* spectral maps differ, several important structures are visible in both (see Figure 7). The most obvious are the comma-shaped cool core and mid-temperature gas northwest of the core, and the low-abundance region corresponding to the 235 MHz radio lobe (around region 3 in Figure 7). The *Chandra* and *XMM* temperature maps also agree well in terms of absolute values, the only significant differences being found in the coolest parts of the cool core, where *Chandra* finds temperatures 0.1-0.2 keV colder than those found by *XMM*.

However, while the *XMM* abundance map does show variations in metallicity within the core, it does not reproduce the clumps of super-solar abundances seen in the *Chandra* map. *Chandra* also finds somewhat higher abundances in the outer part of the core. Differences in background treatment (modelling for *XMM*, blank-sky backgrounds for *Chandra*) seem unlikely to be responsible for this disagreement, given that both datasets are strongly source dominated in this region. Bias associated with multi-phase gas along the line of sight and within spectral extraction regions seems more likely. The *XMM-Newton* spectral extraction regions used in this area range from $16\text{--}44''$ in radius. The smallest regions are comparable in size to the *XMM* point-spread function (PSF), with $16''$ radius corresponding to a 70-75% encircled energy fraction. In the same area, the *Chandra* maps used spectral extraction regions of radius $\sim 4\text{--}40''$, so in the brightest parts of the core, the *Chandra* map will be much less affected by mixing of spectra from regions of differing properties in the plane of the sky, though still affected by multi-temperature gas along the line of sight.

To test the impact of the larger *XMM* extraction regions, we selected five regions from the *XMM* map, and extracted and fitted *Chandra* spectra using the *XMM* extraction regions. Fitting was carried out in XSPEC v12.8.0, in the 0.5-5 keV energy band, using a hydrogen column of $4.94 \times 10^{20} \text{ cm}^{-2}$, matching the values used by David et al. (2011). The regions used are shown in Figure 7 and the fit results are shown in Table 1. In region 2-5 the *Chandra* and *XMM* abundances agree well. In region 1, they agree only at the 2σ level, despite large uncertainties on the *XMM* abundance, but this region is in the coolest part of the cool core, with the most multi-temperature gas along the line of sight. Two tempera-

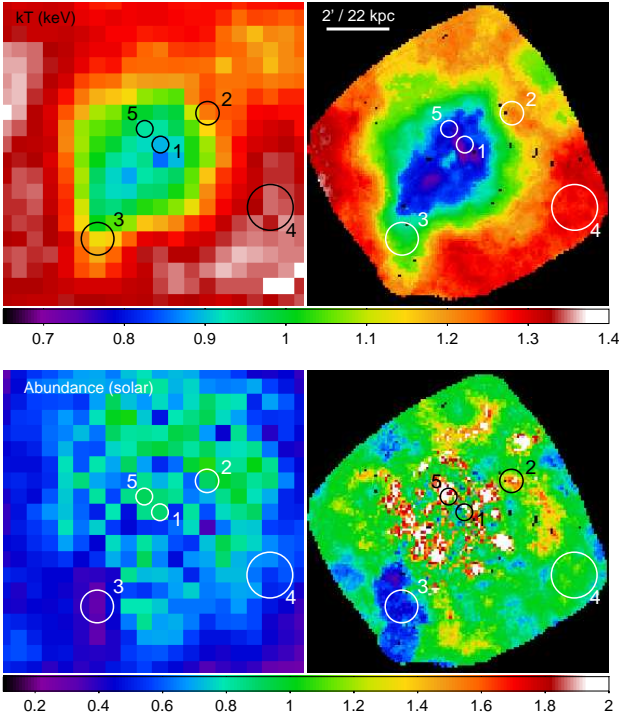


Figure 7. Comparison of *XMM* (left) and *Chandra* ACIS-S3 (right) maps of projected temperature (upper panels) and abundance (lower panels) in NGC 5044. The *Chandra* maps are taken David et al. (2011), and have typical uncertainties of $\sim 3\%$ on temperature and $\sim 35\%$ on abundance. The results of spectral fits to the marked regions are listed in Table 1. Orientation and angular scale of the four images is identical. Note that the colour scales differ from those used elsewhere in this paper.

ture models with abundance linked between the two components provide acceptable fits to the *XMM* data in region 1, 3 and 5, which lie in the cool core and its tail, but do not significantly alter the measured abundance. We therefore conclude that the disagreement between the *Chandra* and *XMM* abundance maps is probably primarily caused by the different spectral extraction region sizes.

4 THE DETACHED RADIO LOBE

Based on spectral fits to *ROSAT* and *Rossini X-ray Timing Explorer* PCA spectra, Henriksen (2011) claimed the detection of spectrally hard non-thermal emission from the NGC 5044 group, with a luminosity of $\sim 2.4 \times 10^{42} \text{ erg s}^{-1}$ within 1° of the dominant galaxy ($\sim 670 \text{ kpc}$, using our chosen distance for luminosity and angular scale). Although their data did not have the spatial resolution to identify the origin of this emission, they suggested that the detached outer radio lobe southeast of NGC 5044 was the most likely source, with the hard component arising from inverse-Compton scattering of cosmic microwave background photons by the relativistic electron population. David et al. (2011) examined *Chandra* spectra from a much smaller, $\sim 15 \times 10 \text{ kpc}$ elliptical region within the lobe and confirmed that the gas in this region was likely multiphase, with a best fit produced by a two-temperature absorbed VAPEC model with Fe and O free to vary independently. The two temperatures, 0.71 and 1.23 keV, are consistent with the range of temperatures observed in the *Chandra* and *XMM* spectral maps and are therefore likely to arise from the IGM surrounding the lobe. The *Chandra*

kT_c (keV)	kT_h (keV)	Fe Z_\odot	O Z_\odot	red. $\chi^2/\text{d.o.f.}$
$0.94^{+0.02}_{-0.08}$	$1.39^{+0.12}_{-0.15}$	$0.80^{+0.12}_{-0.15}$	-	1.0873/803
$0.93^{+0.16}_{-0.18}$	$1.35^{+0.12}_{-0.11}$	$0.68^{+0.07}_{-0.06}$	$0.46^{+0.14}_{-0.12}$	1.0831/802

Table 2. Two-temperature VAPEC fits to the detached lobe region. The upper line shows a fit with all elements fixed in solar ratios, the lower line a fit with Oxygen fitted separately from Fe. The temperature of the cooler component is given by kT_c , while kT_h represents the hotter component.

data showed no indication of any high-temperature or non-thermal component arising from the contents of the radio lobe, but are relatively shallow and insensitive to weak, spectrally hard emission.

The deeper *XMM-Newton* observation provides an opportunity to test again whether any high-temperature component is present. We extracted spectra from a circular region of radius $85''$ ($\sim 16 \text{ kpc}$), chosen to approximate the extent of the radio emission. We also extracted local background spectra from a partial annulus with radii $110\text{--}185''$ between angles of 25 and 250° (measured anti-clockwise from north). This region avoids the tail or spur of cool emission extending from the core toward the lobe, and should approximate the emission along the line of sight to the lobe. To allow a direct comparison with the *Chandra* results, these spectra were initially fitted in the $0.5\text{--}7.0 \text{ keV}$ range with absorption fixed at the Galactic value.

We fitted the spectrum from the lobe with a 2-temperature VAPEC model, initially with all elemental ratios fixed at the solar value, later freeing O to compare with the *Chandra* results of David et al. (2011). Elemental abundances were tied between the two temperature components. The resulting fit parameters are shown in table 2.

The temperatures in the lobe region are somewhat hotter than those found from the *Chandra* data, and when Fe and O are fitted separately the abundances found by both observatories are comparable, though poorly constrained (Fe=0.59-0.86 for *XMM*, 0.71-1.00 for *Chandra*, O=0.31-0.79 for *XMM*, 0.23-0.98 for *Chandra*). Some of these differences may arise from the different *Chandra* and *XMM* extraction regions, and from our use of a local background where David et al. used a blank-sky background.

To search for a spectrally hard non-thermal emission component, we tested single-temperature and two-temperature thermal models with an additional powerlaw component. We fit the MOS and pn spectra in the $0.3\text{--}10 \text{ keV}$ and $0.4\text{--}7.2 \text{ keV}$ bands respectively to take advantage of the high energy sensitivity of *XMM*. We found that a single-temperature-plus-powerlaw model produces a significantly worse fit than the two-temperature thermal model (reduced $\chi^2=1.1156$ for 817 degrees of freedom, compared to 1.0667), with a powerlaw index significantly flatter than that found by Henriksen ($\Gamma=1.56^{+0.31}_{-0.45}$ compared to Henriksen's 2.64-2.82). The flux from the powerlaw is $\sim 3.7 \times 10^{-14} \text{ erg s}^{-1} \text{ cm}^{-2}$ in the $0.5\text{--}15 \text{ keV}$ band used by Henriksen, a factor ~ 365 less than their measurement for the group as a whole. Fitting a two-temperature model with a powerlaw, we found that the best-fitting powerlaw normalisation always approximated zero and the powerlaw index is always poorly constrained; the spectrally soft thermal components account for essentially all the emission detected by *XMM*. The 1σ upper limit on the powerlaw flux fixing $\Gamma=2.7$, approximating Henriksen's best fit value, is $\sim 3 \times 10^{-15} \text{ erg s}^{-1} \text{ cm}^{-2}$.

Taking the flux of the powerlaw in the two-temperature model as an upper limit on the inverse-Compton flux of the lobe, we can place a lower limit on the equipartition magnetic field B_{eq} , based

Region	Extraction Radius (")	XMM 1T		XMM 2T			Chandra map		Chandra spectrum	
		kT (keV)	Abund. (Z_{\odot})	kT _h (keV)	kT _c (keV)	Abund. (Z_{\odot})	kT (keV)	Abund. (Z_{\odot})	kT (keV)	Abund. (Z_{\odot})
1	15.9	0.89±0.01	0.88 ^{+0.02} _{-0.29}	0.93 ^{+0.02} _{-0.10}	0.83 ^{+0.60} _{-0.02}	0.68 ^{+0.23} _{-0.04}	0.69-0.84	0.2-2.7	0.85±0.01	0.47 ^{+0.02} _{-0.03}
2	22.3	1.22 ^{+0.01} _{-0.02}	0.90 ^{+0.25} _{-0.06}	-	-	-	1.12-1.23	1.0-2.4	1.29 ^{+0.02} _{-0.01}	1.11 ^{+0.19} _{-0.15}
3	31.2	1.13 ^{+0.02} _{-0.04}	0.31 ^{+0.46} _{-0.01}	1.29 ^{+0.02} _{-0.03}	0.86 ^{+0.03} _{-0.02}	0.51 ^{+0.48} _{-0.01}	0.92-1.13	0.4-0.9	1.06±0.01	0.34±0.04
4	43.7	1.35 ^{+0.01} _{-0.03}	0.54 ^{+0.15} _{-0.05}	-	-	-	1.25-1.30	0.7-1.2	1.33 ^{+0.02} _{-0.01}	0.71±0.09
5	15.9	0.93±0.01	0.91 ^{+0.03} _{-0.07}	0.73-0.86	0.97 ^{+0.06} _{-0.12}	0.89 ^{+0.11} _{-0.02}	0.68 ^{+0.69} _{-0.01}	1.0-3.3	0.90±0.01	0.84 ^{+0.08} _{-0.07}

Table 1. Temperatures and abundances measured from *XMM* and *Chandra* for the five regions shown in Figure 7. *XMM-Newton* one-temperature (1-T) values are taken from the fits used in making the spectral maps, based on spectra extracted from circular regions whose radius is listed in column 2. Two-temperature (2-T) values use the same spectra and background models. *Chandra* map values indicate the range of temperatures and abundances found within these regions in the ACIS maps, whereas *Chandra* spectrum values are the results of models fitted to ACIS spectra extracted using these regions.

on the ratio of inverse-Compton and synchrotron fluxes (Govoni & Feretti 2004). We measure a 235 MHz flux of 117 mJy at 235 MHz from the GMRT image and adopt the lower limit of $\alpha \geq 1.6$ for the spectral index of the lobe at radio frequencies (David et al. 2009). From these values, we estimate the magnetic field to be $B_{eq} > 3.8 \mu\text{G}$. This is considerably lower than the estimate of $B_{eq} = 23 \mu\text{G}$ found by David et al. (2009) on the basis of pressure equilibrium between the lobe and the surrounding IGM, but this is unsurprising since we were unable to detect a powerlaw component in our two-temperature model. A lower inverse-Compton flux or steeper spectral index would imply a stronger magnetic field. If we adopt $B_{eq} = 23 \mu\text{G}$ as the true magnetic field strength in the lobe, we find that the expected 0.5-15 keV inverse-Compton flux is $\sim 2.7 \times 10^{-17} \text{ erg s}^{-1} \text{ cm}^{-2}$ (or $L_{0.5-15 \text{ keV}} = 5.1 \times 10^{36} \text{ erg s}^{-1}$).

In summary, while these results do not rule out inverse-Compton emission from the lobe, they strongly suggest that it is very weak compared to the thermal emission in the *XMM* band.

5 DISCUSSION AND CONCLUSIONS

It is clear from the abundance map that the sloshing of the NGC 5044 IGM has strongly influenced the distribution of metals. Indeed, although there is a correlation between radio structures, cavities, and abundance in the group core, indicating that nuclear jet activity has affected the abundance distribution, (David et al. 2009, 2011), on larger scales sloshing is much more important than (recent) AGN outbursts in determining the abundance distribution. Numerical modelling of interacting clusters has shown that much of the enriched material transported out from the core to larger radii by sloshing motions will remain at those radii, permanently broadening the abundance distribution (Roediger et al. 2011). It therefore appears that at present, sloshing is the dominant mechanism for transporting metals produced by the stellar population of NGC 5044 out to enrich the IGM, at least on scales ~ 30 -150 kpc.

The lack of any spiral pattern in abundance or temperature, and the presence of secondary abundance clump separated from the core by a lower abundance band, confirms that the orbital plane of perturber is approximately parallel to our line of sight. If the orbital plane were closer to the plane of the sky (perpendicular to our line of sight), we would expect to see a cool, enriched spiral of gas extending out from the core, with a hotter, low abundance spiral extending inward from the IGM. However, while the surface brightness residuals could be considered to contain spiral features, it is clear that the abundance map does not. We must therefore be viewing the sloshing spiral edge-on, with the arm of enriched gas initially extending along the line of sight, curving through the plane of the sky and then arcing back into the line of sight. Our sight

lines can be considered as passing through combinations of cool, enriched “galaxy” gas, and hotter, low-abundance IGM gas. The line of sight through the galaxy passes through both the abundance peak and the base of the uplifted enriched sloshing spiral, combining the highest abundance gas and the greatest depth of enriched gas along the line of sight. The medium-metallicity band in which the 235 MHz detached lobe is found looks through the shortest depth of enriched gas, as the arm of the sloshing spiral is there aligned close to the plane of the sky. The higher abundance clump to the southeast is the tail of the enriched spiral, extended along our line of sight, with a greater depth of enriched gas. Figure 8 illustrates these lines of sight through the group.

From the deprojection analysis of the southeast radial profile shown in Figure 5 we can estimate the density profile, the approximate gas mass and (assuming that Fe emission dominates the abundance measurements) iron mass in each radial bin. The spiral distribution of the sloshing gas is not accounted for by the deprojection, which assumes spherical symmetry and simple radial variations in temperature and abundances, but for our purposes the relatively minor inaccuracies introduced are acceptable. Comparing the differences between the southeast abundance profile with the “undisturbed” mean of the northeast and southwest profiles, and excluding the inner four bins where multi-temperature gas in the core is likely to bias the abundances, we estimate that there is a deficit of $\sim 3.7 \times 10^4 M_{\odot}$ of iron between 125-325", and an excess of $\sim 1.2 \times 10^5 M_{\odot}$ between 325-650". We ignore the outermost bin of the profile since its density is not deprojected and the gas mass would thus be overestimated. These iron masses emphasise that in a sloshing system enriched gas is uplifted from the core; the iron deficit at moderate radii is insufficient to account for the excess at large radii. The sloshing spiral is much broader at small radii than the sector used for spectral extraction, and probably extends further than our profile; these masses are therefore probably underestimates. Nonetheless, sloshing has uplifted a significant mass of enriched gas to at least twice its previous radius.

Precisely estimating the age of the sloshing structures would require a tailored simulation of the NGC 5044 system. Roediger et al. (2012) note that simulations of sloshing in clusters suggest that sloshing fronts expand outward at a relatively constant rate of $\sim 55 \text{ kpc Gyr}^{-1}$, at least for low-mass systems. If this expansion rate holds for NGC 5044, it would suggest ages of 1.2 Gyr and 500 Myr for the two cold fronts. However, the $\sim 150 \text{ km s}^{-1}$ offset of NGC 5044 from the group mean velocity exceeds this expansion rate ($\sim 54 \text{ km s}^{-1}$) by a factor ~ 3 , suggesting that in this case it may be an underestimate. We can estimate (very approximate) ages for the cold fronts based on the local sound speed v_s , assuming the fronts expand at no more than $0.5 \times v_s$. For the outer NW front, the

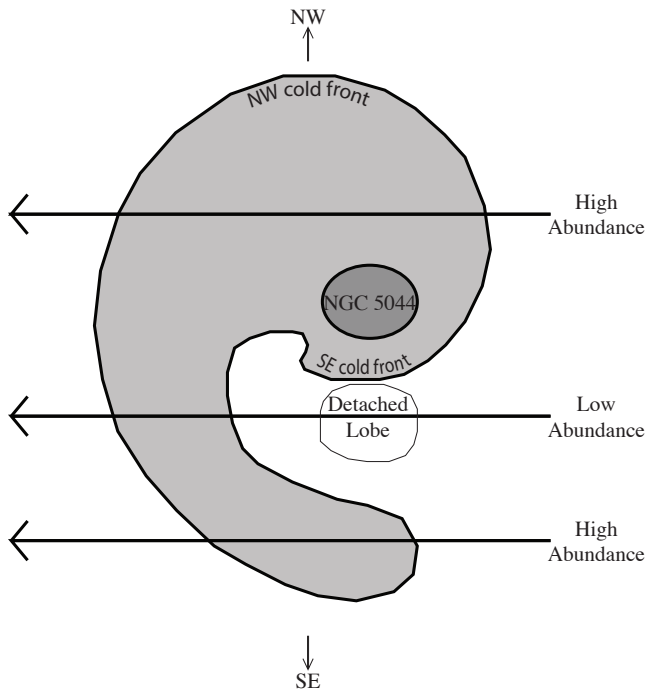


Figure 8. Schematic diagram of the distribution of enriched gas in NGC 5044. Northwest is toward the top of the page, southeast to the bottom, northeast out of the page and southwest into the page. The plane of the sky is perpendicular to the page and the large horizontal arrows, which represent lines of sight from the observer. The light grey region is the enriched “galaxy” gas, surrounded by low metallicity IGM gas (white) and enclosing the NGC 5044 itself (dark grey). Different lines of sight pass through differing amounts of enriched gas producing the projected abundance pattern we observe, with high abundance around the galaxy and in the tail, and low abundance along the line of sight passing through the detached lobe. Note the diagram is not to scale.

local sound speed of $\sim 450 \text{ km s}^{-1}$ suggests a travel time from the group core of 280 Myr. The equivalent values for the inner SE front are 400 km s^{-1} and 140 Myr.

Taking the age of the outer cold front as an indicator of the time since the passage of the perturber through the group core, we can estimate that for a front age of 1.2 Gyr, if NGC 5054 is the cause of the sloshing, it must have a velocity of $\sim 240 \text{ km s}^{-1}$ in the plane of the sky. Alternatively, if the front is only 280 Myr old, the plane-of-sky velocity of NGC 5054 would be $\sim 1050 \text{ km s}^{-1}$. The recession velocity of NGC 5054 is 1075 km s^{-1} less than that of NGC 5044 (Mendel et al. 2008) suggesting that in either case it would have been highly supersonic when passing through the core of NGC 5044.

It is also notable that since the inner cold front appears to have distorted the radio structures visible at 235 MHz, its age may provide a lower limit on the time since the AGN outburst responsible for their formation. 140–500 Myr is an exceptional age for such a small-scale structure, which in a relaxed IGM would be expected to have buoyantly risen out of the core, expanding and fading with time; the sound crossing time between the AGN and lobe is only 20 Myr (David et al. 2009). However, its location between the SE cold front and SE surface brightness excess, in the mixed-abundance band, suggests an explanation of how it has remained (apparently) close to the core. The lobe is probably encapsulated in the arm of hotter, low-abundance IGM gas which has been drawn in toward the group core by the sloshing motion, and the effect of

these large-scale IGM motions has exceeded the buoyant forces which would tend to move the lobe outward. This also explains the strong bending of the 235 MHz jet or filament, which twists around the cold front, probably crossing between the two spirals of enriched outflowing gas, and metal-poor inflowing IGM gas. Increases in pressure associated with these motions or the impingement of the SE cold front onto the inner edge of the lobe may have caused compression of its magnetic field and reacceleration of its particle population, leading to an enhancement of its radio brightness. Unfortunately, confirming the age of the lobe via radio measurements is probably unfeasible. Given the estimated magnetic field of $23 \mu\text{G}$ (David et al. 2009), and conservatively assuming no energy losses from adiabatic expansion or inverse-Compton scattering, we would expect the break in the spectral index of the radio emission to be at (or below) $\sim 0.8\text{--}10 \text{ MHz}$, below the observable waveband of current observatories.

Acknowledgements

We thank the anonymous referee for a rapid and thorough reading of the paper. This work is based on observations obtained with XMM-Newton, an ESA science mission with instruments and contributions directly funded by ESA Member States and NASA. Support for the analysis was provided by the National Aeronautics and Space Administration through the Astrophysical Data Analysis programme, award NNX13AE71G.

REFERENCES

- Arnaud K. A., 1996, in Jacoby G. H., Barnes J., eds, *Astronomical Data Analysis Software and Systems V* Vol. 101 of *Astronomical Society of the Pacific Conference Series*, XSPEC: The First Ten Years. p. 17
- Ascasibar Y., Markevitch M., 2006, *ApJ*, 650, 102
- Buote D., Fabian A., 1998, *MNRAS*, 296, 977
- Buote D. A., Lewis A. D., Brighenti F., Mathews W. G., 2003a, *ApJ*, 594, 741
- Buote D. A., Lewis A. D., Brighenti F., Mathews W. G., 2003b, *ApJ*, 595, 151
- Canning R. E. A., Sun M., Sanders J. S., Clarke T. E., Fabian A. C., Giacintucci S., Lal D. V., Werner N., Allen S. W., Donahue M., Johnstone R. M., Nulsen P. E. J., Sarazin C. L., 2013, arXiv:1305.0050
- Cellone S. A., Buzzoni A., 2005, *MNRAS*, 356, 41
- David L. P., Jones C., Forman W., Daines S., 1994, *ApJ*, 428, 544
- David L. P., Jones C., Forman W., Nulsen P., Vrtilek J., O’Sullivan E., Giacintucci S., Raychaudhury S., 2009, *ApJ*, 705, 624
- David L. P., O’Sullivan E., Jones C., Giacintucci S., Vrtilek J., Raychaudhury S., Nulsen P. E. J., Forman W., Sun M., Donahue M., 2011, *ApJ*, 728, 162
- de Plaa J., Werner N., Simionescu A., Kaastra J. S., Grange Y. G., Vink J., 2010, *A&A*, 523, A81
- Freeman P., Doe S., Siemiginowska A., 2001, in J.-L. Starck & F. D. Murtagh ed., *Society of Photo-Optical Instrumentation Engineers (SPIE) Conference Series* Vol. 4477 of *Society of Photo-Optical Instrumentation Engineers (SPIE) Conference Series*, *Sherpa: a mission-independent data analysis application*. p. 76
- Gastaldello F., Buote D. A., Temi P., Brighenti F., Mathews W. G., Etori S., 2009, *ApJ*, 693, 43
- Gastaldello F., Di Gesu L., Ghizzardi S., Giacintucci S., Girardi M., Roediger E., Rossetti M., Brighenti F., Buote D. A., Eckert D., Etori S., Humphrey P. J., Mathews W. G., 2013, *ApJ*, 770, 56

- Ghizzardi S., De Grandi S., Molendi S., 2013, *Astron. Nachr.*, 334, 422
- Govoni F., Feretti L., 2004, *International Journal of Modern Physics D*, 13, 1549
- Grevesse N., Sauval A. J., 1998, *Space Sci. Rev.*, 85, 161
- Henriksen M. J., 2011, *ApJ*, 726, 9
- Kalberla P. M. W., Burton W. B., Hartmann D., Arnal E. M., Bajaja E., Morras R., Pöppel W. G. L., 2005, *A&A*, 440, 775
- Kirkpatrick C. C., Gitti M., Cavagnolo K. W., McNamara B. R., David L. P., Nulsen P. E. J., Wise M. W., 2009, *ApJ*, 707, L69
- Markevitch M., Ponman T. J., Nulsen P. E. J., Bautz M. W., Burke D. J., David L. P., Davis D., Donnelly R. H., Forman W. R., Jones C., Kaastra J., Kellogg E., Kim D.-W., et al. 2000, *ApJ*, 541, 542
- Markevitch M., Vikhlinin A., 2007, *Phys. Rep.*, 443, 1
- Markevitch M., Vikhlinin A., Mazzotta P., 2001, *ApJ*, 562, L153
- Mendel J. T., Proctor R. N., Forbes D. A., Brough S., 2008, *MNRAS*, 389, 749
- O'Sullivan E., Giacintucci S., Babul A., Raychaudhury S., Venturi T., Bildfell C., Mahdavi A., Oonk J. B. R., Murray N., Hoekstra H., Donahue M., 2012, *MNRAS*, 424, 2971
- O'Sullivan E., Giacintucci S., David L. P., Gitti M., Vrtilek J. M., Raychaudhury S., Ponman T. J., 2011, *ArXiv e-prints*, 735, 11
- O'Sullivan E., Giacintucci S., David L. P., Vrtilek J. M., Raychaudhury S., 2011, *MNRAS*, 411, 1833
- O'Sullivan E., Vrtilek J. M., Harris D. E., Ponman T. J., 2007, *ApJ*, 658, 299
- Roediger E., Brügggen M., Simionescu A., Böhringer H., Churazov E., Forman W. R., 2011, *MNRAS*, 413, 2057
- Roediger E., Kraft R. P., Machacek M. E., Forman W. R., Nulsen P. E. J., Jones C., Murray S. S., 2012, *ApJ*, 754, 147
- Sanders J. S., Fabian A. C., Allen S. W., Schmidt R. W., 2004, *MNRAS*, 349, 952
- Simionescu A., Werner N., Forman W. R., Miller E. D., Takei Y., Böhringer H., Churazov E., Nulsen P. E. J., 2010, *MNRAS*, 405, 91
- Snowden S. L., Collier M. R., Kuntz K. D., 2004, *ApJ*, 610, 1182
- Tamura T., Kaastra J. S., Makishima K., Takahashi I., 2003, *A&A*, 399, 497
- Vikhlinin A., Markevitch M., Murray S. S., 2001, *ApJ*, 551, 160
- ZuHone J. A., Markevitch M., Lee D., 2011, *ApJ*, 743, 16